

# The Effects of Bottom Blowing Gas Flow Rate Distribution During the Steelmaking Converter Process on Mixing Efficiency



KUAN-YU CHU, HSING-HAO CHEN, PO-HAN LAI, HSUAN-CHUNG WU,  
YUNG-CHANG LIU, CHI-CHENG LIN, and MUH-JUNG LU

Featuring the advantages of top-blown and bottom-blown oxygen converters, top and bottom combined blown converters are mainstream devices used in steelmaking converter. This study adopted the FLUENT software to develop a numerical model that simulates 3D multiphase flows of gas (air and argon), liquid steel, and slag. Ten numerical experiments were conducted to analyze the effects that the bottom blowing gas flow rate distribution patterns (uniform, linear fixed total flow rate, linear fixed maximal flow rate, and V-type) and bottom blowing gas flow distribution gradients of combined blown converters exert on slag surface stirring heights, flow field patterns, simulation system dynamic pressures, mixing time, and liquid steel–slag interface velocity. The simulation results indicated that the mixing efficiency was highest for the linear fixed total flow rate, followed by the linear fixed maximal flow rate, V-type, and uniform patterns. The bottom blowing gas flow rate distribution exhibited linear patterns and large gradients, and high bottom blowing total flow rates increased the mixing efficiency substantially. In addition, the results suggested that even when bottom blowing total flow rate was reduced, adopting effective bottom blowing gas flow rate distribution patterns and gradients could improve the mixing efficiency.

DOI: 10.1007/s11663-016-0593-1

© The Minerals, Metals & Materials Society and ASM International 2016

## I. INTRODUCTION

MOLTEN iron produced in a blast furnace contains a considerable amount of impure elements, such as carbon, silicon, magnesium, phosphorus, and sulfur, and features rigid but brittle properties that hinder processing. Steelmaking is a refining process in which oxidation is used as the primary measure and oxygen is employed to oxidize and separate impurities in molten iron and control the liquid steel properties to conform to product specifications. A converter steelmaking method uses the reactions occurring between oxygen and impurities to form slag and increases the molten steel temperature by using the oxidization heat of impurities. The slag is then removed, completing the refined and rapid steelmaking.

According to the classification of gas blowing parts, converters can be classified into top-blown converters,<sup>[1]</sup> bottom-blown converters,<sup>[2]</sup> and top and bottom

combined blown converters.<sup>[3]</sup> The blowing point of pure oxygen top-blown converters concentrates, causing ineffective liquid steel mixing. Thus, the various reactions between the blown oxygen and liquid steel, and between the liquid steel and slag are insufficient and nonuniform. The bottom-blown converters development was to improve the disadvantages of top-blown converters. The advantages of the bottom-blown method include efficient mixing, a large contact area between oxygen and liquid steel, and rapid chemical reactions. However, the bottom-blown method reduces refractory material lifetime because the high-temperature area is located at the bottom of the converter. During the production process, the top and bottom combined blown converters use top-blown oxygen to react with liquid steel, and bottom blowing is used to blow inert gases into the liquid steel. The initial kinetic energy from the gases and the kinetic energy increased during the bubble rising process can activate the flow field in the converter, uniformly mixing the oxygen and impurities in the liquid steel, and thereby reducing the impurities. Featuring the advantages of both top-blown and bottom-blown converters, top and bottom combined blown converters have become the current dominant converters.

There has been much research regarding the combined blown converters in both CFD and physical modeling conducted in past decades. Li *et al.*<sup>[4]</sup> used multiphase flow models combined a discrete phase model and VOF to describe the gas and liquid two phase flow in the combined blown converters. The

KUAN-YU CHU and HSING-HAO CHEN, Graduate Students, PO-HAN LAI, University Student, and HSUAN-CHUNG WU, Associate Professor, are with the Department of Materials Engineering, Ming Chi University of Technology, 84 Gungjuan Road, Taishan, New Taipei 24301, Taiwan. Contact e-mail: hcwu@mail.mcut.edu.tw; h.c.wu2015@gmail.com YUNG-CHANG LIU, Scientist, CHI-CHENG LIN, Engineer, and MUH-JUNG LU, Assistant General Manager, are with the Iron & Steel Research & Development Department, China Steel Corporation, 1 Chung Kang Road, Hsiao Kang, Kaohsiung 81233, Taiwan.

Manuscript submitted on April 10, 2015.

Article published online February 1, 2016.

results showed that the stirring energy in the combined blowing converter is dominated by buoyancy-driven bottom blowing bubbles. Lv *et al.*<sup>[5]</sup> found that the diameter of impinging cavity on the slag and steel surface decreases with an increase in the slag thickness. Li *et al.*<sup>[6]</sup> indicated the total momentum transferred from the top jets into the bath is consumed about a half to drive the movement of slag, rather than fully converted as the stirring energy for the liquid steel. Zhou *et al.*<sup>[7]</sup> applied a mathematical model to study the kinetic energy transfer from a top and bottom gas injection to the liquid steel in the converter. They indicated that the energy transfer for the bottom blowing is much more efficient than that of the top blowing. Zhong *et al.*<sup>[8]</sup> used physical modeling experiments to study the effect of blowing process parameters and represented that bottom gas injection benefits mixing in top–bottom-side blown converters.

In recent years, some studies have explored how to improve the mixing efficiency of top and bottom combined blown converters. Among the proposed methods, adjusting manufacturing process parameters relevant to the bottom blowing tuyere has been the most effective. Ganguly *et al.*<sup>[9]</sup> used physical and mathematical models to analyze the effect a single tuyere located at 0, 0.5, and 0.75  $R$  ( $R$ , radius of converter bottom) in a cylindrical container (diameter, 0.63 m; height, 0.58 m) exerted on mixing time. The results revealed that when the bottom blowing gas flow rate increased, the mixing time decreased. When the bottom tuyere was positioned at 0.5  $R$ , the minimal mixing time was obtained. Based on the symmetry of the bottom tuyere positions and their distance from the converter bottom center, and the distances between the bottom tuyeres, Choudhary *et al.*<sup>[10]</sup> used a combined blown converter water model with eight bottom tuyeres to analyze the effect of ten bottom tuyere positions on mixing time. The experimental results indicated that the bottom tuyeres positioned at diverse intervals reduced the mixing time. Singh *et al.*<sup>[11]</sup> used water and mathematical models to simulate a combined blown converter and bottom-blown converter with eight bottom tuyeres. The pitch circle ratios (PCRs) of the eight tuyeres were 0.4, 0.5, 0.58, and 0.66. The results suggested that the combined blown converter and bottom-blown converter achieved a minimal mixing time when the PCRs were 0.4 and 0.5, respectively. Subsequently, a mathematical simulation involving the use of PCR range from 0.5 to 0.58 showed that a minimal mixing time was obtained when PCR was 0.56. In addition, Singh *et al.*<sup>[12]</sup> used a water model to simulate a top and bottom combined blown converter with eight bottom tuyeres, exploring the effect four patterns of bottom tuyere flow rate distribution (uniform, linear, V-type, and M-type) exerted on the mixing time. The results indicated that when the flow rate distribution was in a linear pattern, the mixing time was 30–35 pct less than that when the distribution was uniform. The V-type and M-type patterns decreased the mixing time by approximately 5 pct compared with the uniform pattern. Studies have suggested that applying linear distribution patterns for bottom tuyere flow rates to manufacturing processes can

effectively increase the dephosphorization efficiency. In 2008, Lai *et al.*<sup>[13]</sup> used a water model to simulate combined blown converters with three to six bottom tuyeres and investigated the effect the bottom tuyere position (symmetrical, concentrated) exerted on mixing time. The experimental results revealed that when the bottom tuyeres were arranged ineffectively, increased flow rates did not reduce the mixing time. When the bottom tuyere positions were concentrated, the mixing energy barrier was lowered. The mixing time of unsymmetrically arranged bottom tuyeres was shorter than that of symmetrically arranged tuyeres, because the unsymmetrical arrangement enhanced horizontal flows.

According to a bottom tuyere design perspective, previous studies have indicated that if the flow field distribution generated by bottom-blown gases creates velocity gradients in a radial direction, the mixing efficiency can be enhanced. These radial velocity gradients can be achieved through two methods: (1) designing the arrangement of bottom tuyeres, and (2) controlling the flow rate of each bottom tuyere. When ease of on-site variation is crucial, changing and analyzing the effect the flow rate distribution exerts on mixing efficiency should be the optimal method.

This study adopted the FLUENT software to simulate and analyze the effect the bottom flow rate distributions in combined blown converters exert on mixing efficiency. The study first established a 3D multiphase flow numerical model that can simulate gases (air and argon), liquid steel, and slag, and then calculated the mixing time, facilitating the evaluation of process performance. This 3D multiphase flow simulation system was used to calculate the mixing time of various process conditions based on the different flow rate distribution patterns of bottom tuyeres (uniform, linear fixed total flow rate, linear fixed maximal flow rate, and V-type) and gradients to analyze the mixing efficiency. In addition, the flow field variations inside the converters and the liquid steel and slag stirring were observed.

## II. THEORETICAL BASIS

The numerical model of a combined blown converter process is considerably complex, including the thermodynamic and kinetic reactions occurring between oxygen and carbon, silicon, magnesium, phosphorus, and sulfur in liquid steel; the fluid dynamics and heat and mass transfer phenomena between gases and liquid steel. This study considered only the flow phenomenon occurring between gases, liquid steel, and slag. The following assumptions are proposed.

- (1) Liquid steel temperature is fixed at 1873 K (1600 °C).
- (2) The liquid steel is Newtonian fluid with a fixed viscosity value.
- (3) Fluid is incompressible

The involved transfer phenomena include gas and liquid steel flow, gas-resulting stirring in liquid steel and slag, and surface splashing problems; the transfer is a multiphase flow problem. Thus, a mathematical model

and numerical analysis must be able to calculate the multiphase flow (air, argon, liquid steel, and slag) and free surface. The commercial package software FLUENT, which is able to calculate multiphysics, was adopted in this study because FLUENT can address gas–liquid coexistence, track multiphase interface positions, and calculate mixing time by using mass transfer. The main control equations of fluid flow<sup>[14]</sup> were as follows:

Continuity

$$\frac{\partial \rho}{\partial t} + \nabla \cdot (\rho \vec{V}) = S_m \quad [1]$$

Momentum

$$\begin{aligned} \frac{\partial}{\partial t} (\rho \vec{V}) + \nabla \cdot (\rho \vec{V} \vec{V}) = & -\nabla p + \nabla \cdot [\mu (\nabla \vec{V} + \nabla \vec{V}^T)] \\ & + \rho \vec{g} + \vec{F}, \end{aligned} \quad [2]$$

where  $\rho$  is density;  $t$  is time;  $\vec{V}$  is the velocity vector;  $S_m$  represents source terms;  $p$  is pressure;  $\mu$  is viscosity;  $\vec{g}$  is gravitational acceleration; and  $\vec{F}$  is body force. The weighted average density and viscosity in each grid were calculated using the volume fraction  $\alpha_q$  of each phase in the grid.

The standard  $k-\varepsilon$  model<sup>[15]</sup> was used to model turbulence. To address the surface tension, a continuum surface force (CSF) model was used.<sup>[16]</sup> The CSF model considers surface tension as a continual force crossing the interface, expressed in Eq. [3].

$$\vec{F}_s = \sigma \kappa \nabla \alpha, \quad [3]$$

where  $\vec{F}_s$  is the body force caused by surface tension;  $\sigma$  is the surface tension coefficient;  $\alpha$  is the liquid volume fraction; and  $\kappa$  is the gas–liquid interface curvature that is directionally oriented to the center of liquid curvature, which is expressed in Eq. [4]

$$\kappa = - \left( \nabla \cdot \frac{\vec{n}}{|\vec{n}|} \right), \quad [4]$$

where  $\vec{n}$  is the normal vector of the gas–liquid interface that is directionally oriented to the center of liquid curvature. The normal vector is expressed in Eq. [5]:

$$\vec{n} = \nabla \alpha. \quad [5]$$

Multiphase flows were calculated using the volume of fluid (VOF) method,<sup>[17,18]</sup> which tracks the free surface variation and morphology based on the concept of fluid volume fraction. For interface reconstruction, the piecewise linear interface calculation (PLIC) method proposed by Youngs was adopted.<sup>[19–21]</sup> The interface within the grids was expressed using a plane in arbitrary direction; the plane direction was determined based on the fluids in nearby grids. This method includes three steps:

- (1) Build or reconstruct the interface.
- (2) Calculate the velocity field.
- (3) Calculate the transfer of the  $\alpha$  value and the distribution after the  $\alpha$  value is transferred.

Figure 1 depicts a geometric diagram of the simulated area in a 150t converter. The diameter of the bottom tuyere was 80 mm. This study mainly analyzed the effect that bottom flow rate distributions in combined blown converters exert on the mixing efficiency and, therefore, the top blowing section was not considered. The external shape and process conditions of the converter were biaxial symmetric. To improve the computational efficiency of 3D simulation, a symmetry plane was used for calculations. The symmetry plane is considered a zero flux boundary for mass and momentum transfer. The bottom wall and surrounding surfaces adopted no-slip boundary condition. The top surface used open boundary. The gas injection from a tuyere (Figure 1(b)) is assumed to have the uniform velocity magnitude.

The grids of the entire simulation system were tetrahedrons featuring side lengths of 50 mm. To accurately calculate the flow fields near the bottom tuyeres, six grid nodes spaced at an interval of approximately 42 mm on the circumference of the tuyere circle

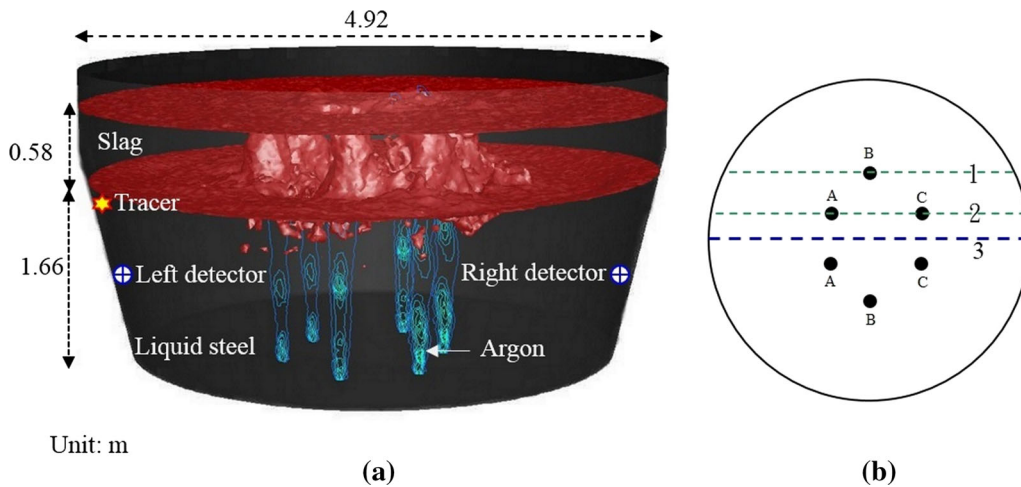


Fig. 1—(a) Converter dimensions and initial height of liquid steel–slag in the simulation system; (b) tuyere position at the bottom of the converter.

**Table I. Physical Properties of Liquid Steel, Slag, and Argon**

Physical Property	Liquid Steel	Slag	Argon
Density (kg/m <sup>3</sup> )	6932	3490	0.4836
Viscosity (kg/m s)	$5.1 \times 10^{-3}$	0.1	$4.66 \times 10^{-5}$
Surface tension (N/m)	liquid steel–gas and slag–gas: 1.54		

**Table II. Bottom Blowing Conditions of Ten Cases (Including the Bottom Blowing Gas Flow Rate Distribution with a Uniform Pattern, Linear Fixed Total Flow Rate at 480 Nm<sup>3</sup>/h, Linear Fixed Bottom Tuyere Maximal Flow Rate at 80 Nm<sup>3</sup>/h, and V-Type Pattern)**

Types of Bottom Flow Rate		Total Flow Rate (Nm <sup>3</sup> /h)	Flow Rate Per Tuyere (A-B-C) (Nm <sup>3</sup> /h)
STD	uniform	480	80-80-80
Case1	linear	480	60-80-100
Case2			40-80-120
Case3			20-80-140
Case4	linear	420	60-70-80
Case5		360	40-60-80
Case6		300	20-50-80
Case7	V-type	480	90-60-90
Case8			100-40-100
Case9			110-20-110

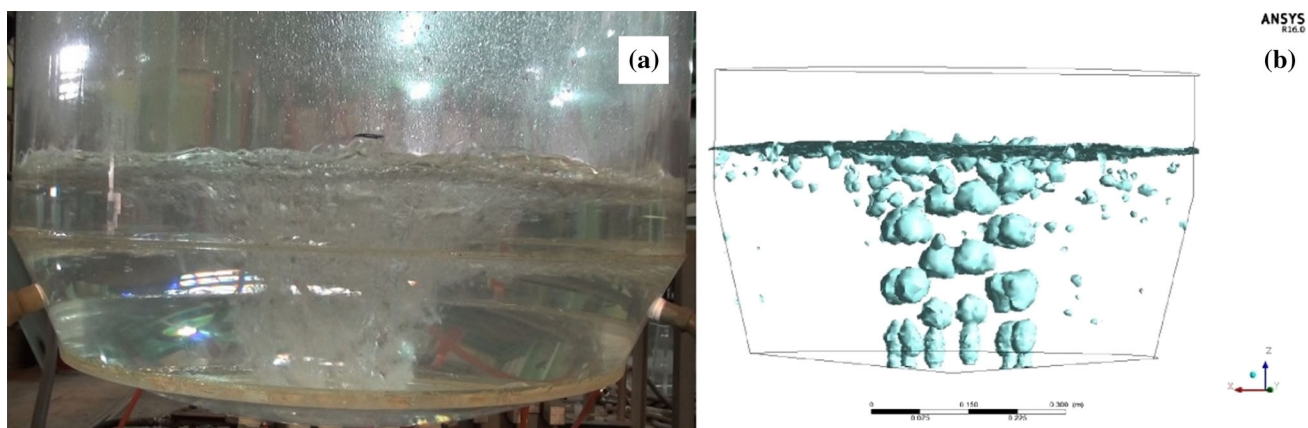


Fig. 2—Comparison of the simulated result with experimental photograph (six tuyeres and a gas flow rate of 25 N ℓ/min for each tuyere) (a) experimental photograph; (b) simulated result.

were established. The entire system included approximately 1.15 million grids.

### III. RESULTS AND DISCUSSION

Table I shows the physical properties of liquid steel, and slag that were determined from literature.<sup>[22]</sup> The density of argon was estimated from the ideal gas law. Table II shows the ten numerical experimental cases that were examined in this study. Figure 1(b) shows tuyere position at the bottom of the converter. The bottom blowing conditions of STD were used as the reference case: six bottom tuyeres were used, and the flow rate per tuyere was 80 Nm<sup>3</sup>/h. When the fixed total gas flow rate was 480 Nm<sup>3</sup>/h, the bottom blowing flow rates of Cases 1 to 3 (Part 1) exhibited linear distribution

and the flow rate gradients increased sequentially. Although the bottom blowing flow rate of Cases 4 to 6 (Part 2) also exhibited linear distribution and sequential increase in flow rate gradient, the fixed bottom blowing maximal flow rate of a single tuyere was set at 80 Nm<sup>3</sup>/h and the total bottom-blown gas flow rates in Cases 4, 5, and 6 were 420, 360, and 300 Nm<sup>3</sup>/h, respectively. When the fixed total flow rate of gas was 480 Nm<sup>3</sup>/h, the bottom blowing flow rates of Cases 7 to 9 (Part 3) exhibited V-type distribution, and the flow rate gradients increased sequentially. The calculation process consisted of two steps. First, the steady state flow field (30 seconds) of each case was obtained. Second, tracers and detection points were placed in the steady state flow field as shown in Figure 1(a) to record the time-varying tracer concentrations of detection points. Consequently, the mixing time of the system

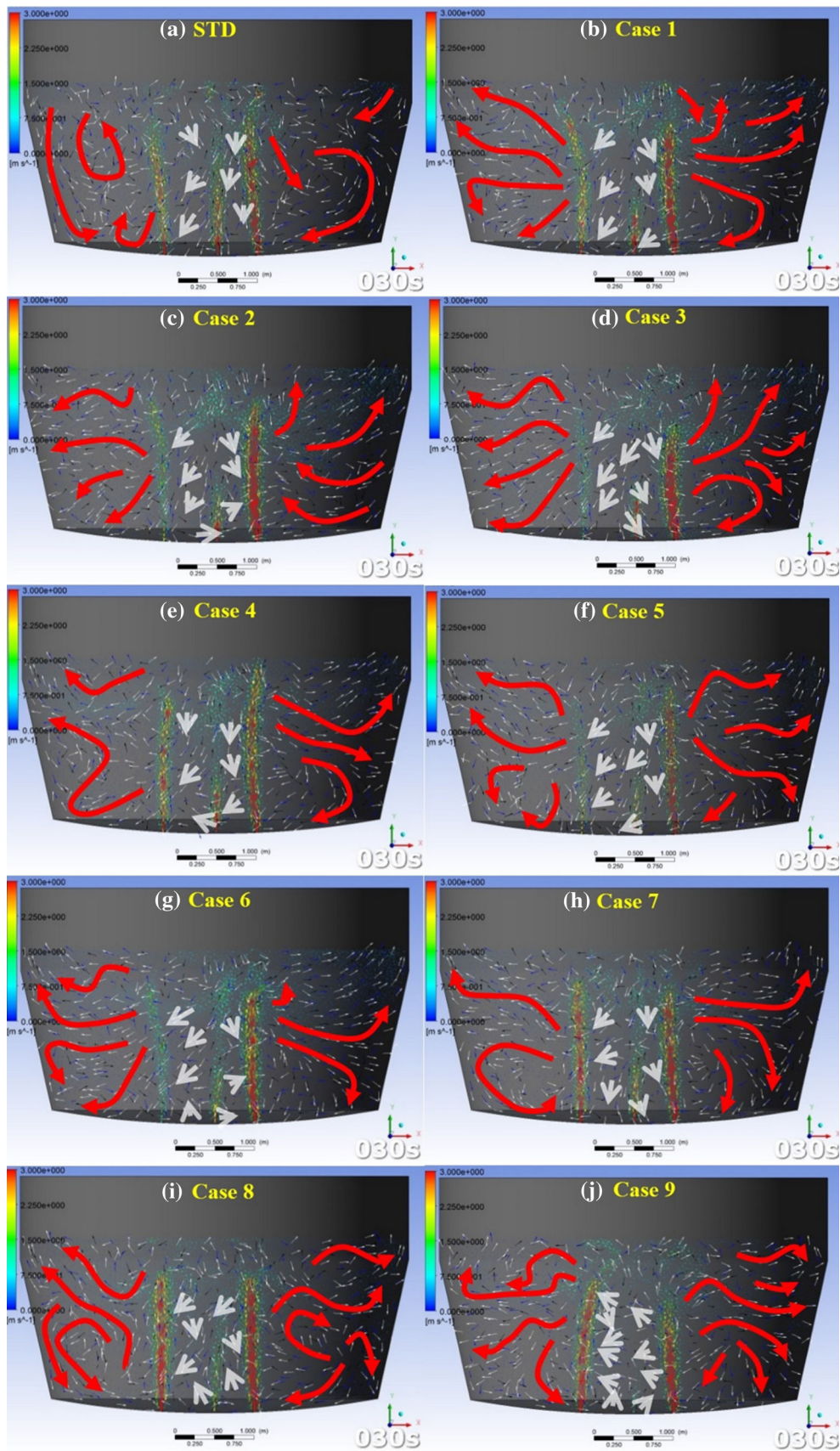


Fig. 3—Velocity fields of three cross sections at 30 s.

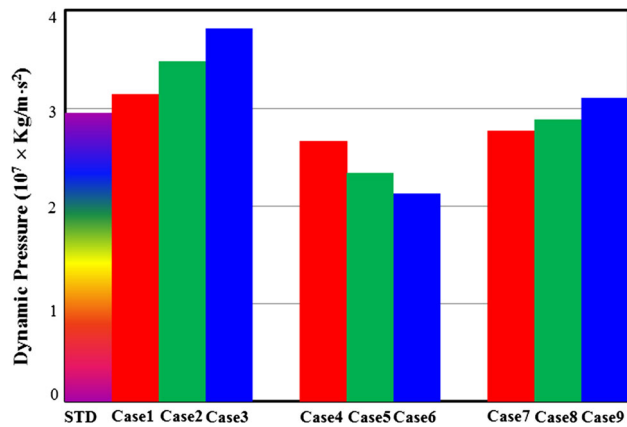


Fig. 4—Average dynamic pressure of liquid steel + slag systems obtained during 0 to 30 seconds in the ten cases.

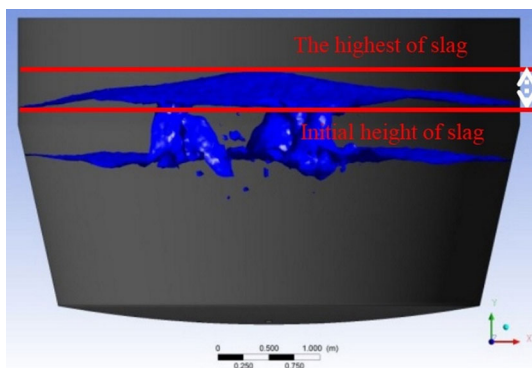


Fig. 5—Schematic diagram of calculated slag surface stirring height.

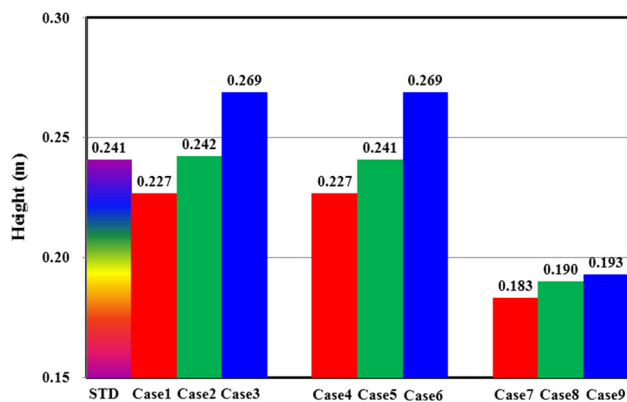


Fig. 6—Highest stirring height of slag surfaces between 0 and 30 s.

and the velocity and dynamic pressure of the liquid steel–slag interface were calculated.

#### A. Verification of the Simulation System

For the numerical model verification, the experiments of water model were performed by scaling down the 150t converter by 6.5 times. In the experiment, water and air

are used to represent liquid steel and argon, respectively. A photograph is taken when the water model is bottom-blown with a gas flow rate of 25 N ℓ/min for each tuyere as shown in Figure 2(a). The stirring phenomena and the distribution of gas bubbles can be clearly seen from the photograph. Accordingly, the water model is simulated by the present numerical model with all the parameters corresponding to the related process conditions as shown in Figure 2(b). Overall, when the two results are compared, good consistency can be observed, which assures the reliability of the simulation system.

#### B. Flow Field Pattern

If all velocity vectors inside a 3D converter are depicted, the flow field graph will be too disorganized to observe. Thus, during velocity field analysis, only the symmetry plane of the converter and the cross sections vertical to the bottom tuyeres were extracted. Figure 1(b) shows the three extracted sections, which are indicated by dotted lines. A flow field pattern from 0 to 30 seconds was observed. The velocity vectors in Section I through III are indicated using black, blue, and white arrows, respectively.

Figure 3 depicts velocity fields (30 seconds) that were used to explain the flow field characteristics among the ten cases. The large white arrow in Figure 3 indicates the flow field tendency of the inner circle of the six bottom tuyeres, and the large red arrows show the flow field tendency of the external circle of the six tuyeres. In the inner circle, downward vertical components accounted for most of the STD flow field. The flow field in Part 1 exhibited large horizontal components, particularly in Cases 2 and 3 with large gradients, in which nearly horizontal flow fields were observed at the bottom of the converters. In addition, the color gradients indicated that in Cases 1 to 3, the flow velocity above the right-side bottom tuyeres was higher than that above the middle and left side. In the external circles, the STD flow field featured a circular pattern, whereas the flow fields in Part 1 were in radial patterns. Because the bottom blowing flow rate distribution exhibited linear patterns in Part 2, the flow field patterns were similar to those in Part 1. Comparing the distribution pattern in Part 3 with the linear distribution patterns (Parts 1 and 2) indicated that in Part 3, increased upward flow fields existed in the inner circle of the bottom tuyeres.

Figure 4 shows the average dynamic pressure of the (liquid steel + slag) system from 0 to 30 seconds. The average dynamic pressure was calculated by averaging the dynamic pressure (kinetic energy per unit volume) at transient time points in the simulation system. The results showed that the bottom blowing total gas flow rate, flow rate distribution patterns, and flow rate distribution gradients affected the system dynamic pressures. When total flow rate was the same, the increasing gradients of bottom blowing flow rate distribution and the increasing flow rate of a single bottom blowing tuyere on the right side in Cases 1 to 3 increased the system dynamic pressures. Comparing Cases 4 to 6 determined that the system dynamic pressures decreased

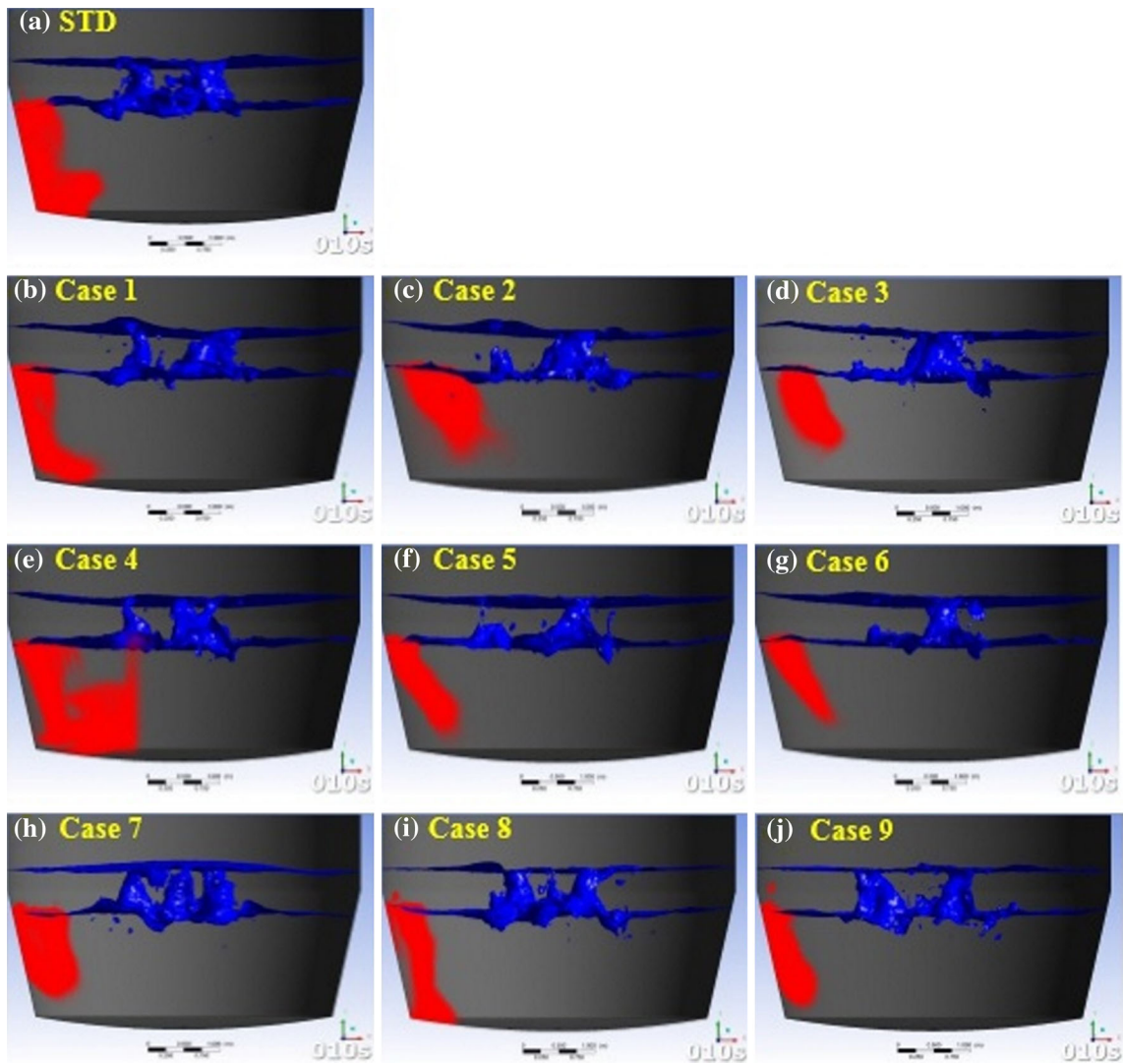


Fig. 7—Distribution of the tracer concentration at 10 s in the ten cases.

with the decreasing total flow rate. Comparing Part 1 with Part 3 suggests that when total flow rate conditions were the same, the linear pattern of bottom blowing flow rate distribution had higher dynamic pressures compared with the V-type patterns.

### C. Slag Surface Stirring Height

To evaluate the degree of slag splash, the stirring height was quantitatively calculated, as shown in Figure 5. The STD was used to illustrate the calculation method of slag surface stirring heights. First, grids with slag volume fractions  $\geq 0.5$  in each time period were selected, and the maximum of the vertical coordinate of these grids was determined. Finally, the slag surface stirring height at a set time was identified by subtracting the initial slag surface height from the maximal value. Figure 6 shows the calculation results of the slag surface stirring heights, which ranged between 0.183 and 0.269 m. The bottom blowing distribution patterns were

linear in Parts 1 and 2. Although the bottom blowing total flow rate of Part 2 was lower than that of Part 1, the slag surface stirring heights of both Parts 1 and 2 approximated and were higher than that of Part 3. This result indicated that the bottom blowing flow rate distribution patterns were the primary factors influencing the stirring heights. In addition, large bottom blowing flow rates did not necessarily cause considerable stirring. The slag surface stirring heights of Parts 1 and 3 under a fixed bottom blowing total flow rate increased with the bottom blowing flow rate distribution gradients. Cases 4 to 6 in Part 2 suggested that despite the decreased total flow rate, the increased bottom blowing flow rate distribution gradients resulted in substantial slag surface stirring. This result revealed that when the bottom blowing flow rate distribution was in a V-type pattern, the slag surface stirring was smaller.

When the bottom blowing is performed only in a single tuyere, the surface stirring height is expected to increase with the flow rate. However, the calculation

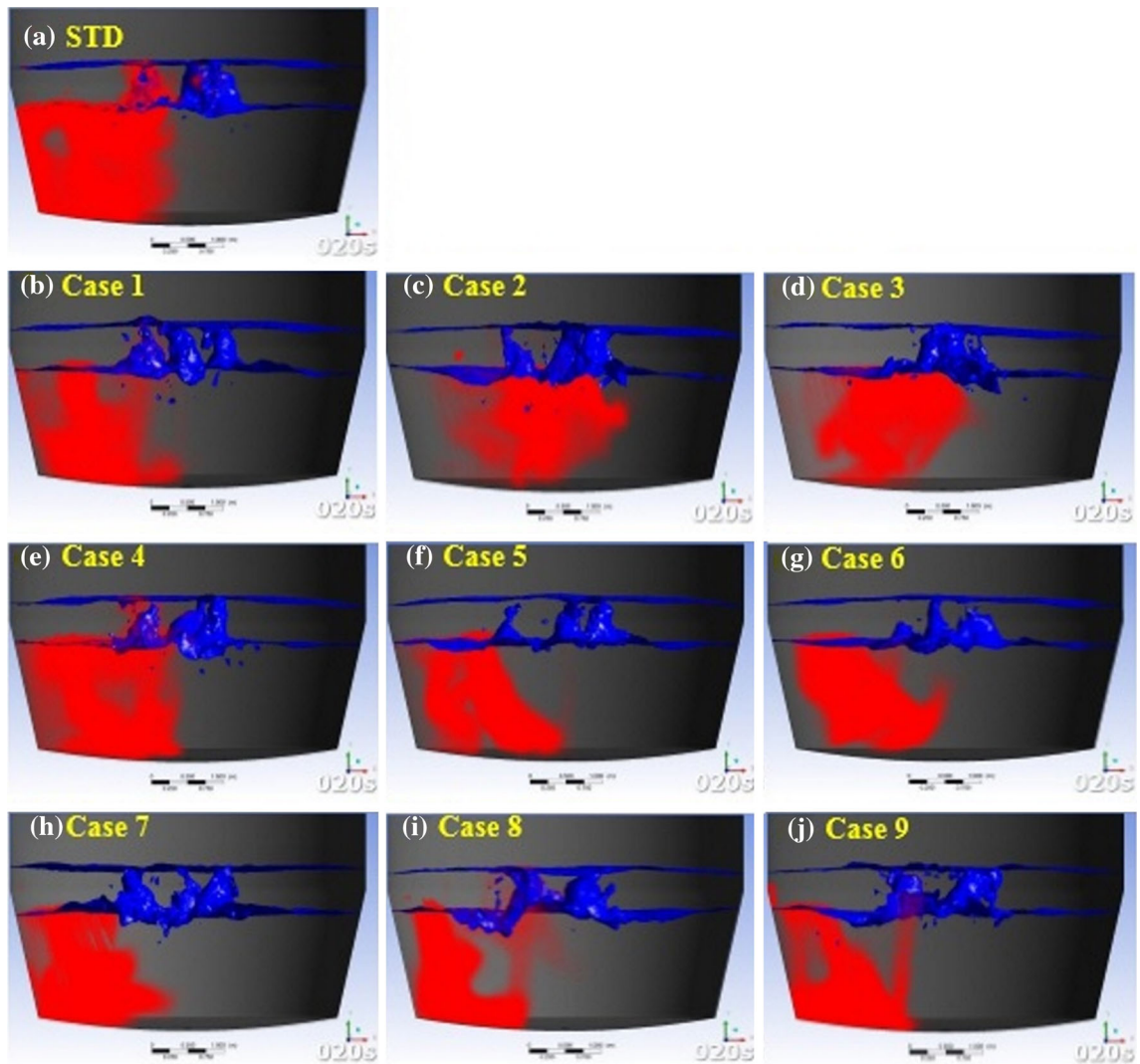


Fig. 8—Distribution of the tracer concentration at 20 s in the ten cases.

results derived from the six bottom tuyeres suggested that the slag surface stirring heights were primarily affected by the bottom blowing flow rate distribution patterns and gradients, instead of the bottom blowing total flow rates. This phenomenon was possibly caused by the mutual effect among flow fields resulting from each bottom tuyeres. Among the distribution patterns, the linear patterns generated more substantial stirring compared with the V-type pattern. Under the same distribution pattern, larger flow rate gradients caused more stirring.

#### D. Mixing Time

In each case, the simulation results at 30 seconds were used as the initial condition to calculate the mixing time. The time then was zeroed to compute the mixing time. Figure 1 shows the positions of one tracer and two detection points. The property of tracer is the same as the liquid steel shown in Table I. The tracer was

positioned just below the slag, near the left converter wall. A detection point was set on the left and right sides at the half-liquid height.

Figures 7 through 12 depict the tracer variations with the flow field at times of 10, 20, 30, 40, 60, and 80 seconds. The red color indicated the tracer, and the dark color represented the concentration level. At 10 seconds (Figure 7), the tracer in Cases 2, 3, 5, and 6 exhibited linear bottom blowing flow rate distribution patterns and large gradients mainly flowed to the right side of the converter. The tracer in other cases typically flowed down along the converter wall toward the bottom. At 20 seconds (Figure 8), the tracer in Cases 2 to 6 with linear bottom blowing flow rate distribution patterns approached or passed the converter center. In addition, the tracer flow was the fastest in Cases 2 and 3. Most of the tracer in the V-type pattern was distributed in the left side of the left-side bottom tuyeres at 20 seconds. At 30 seconds (Figure 9), the tracer in Cases 2 to 6 flowed to the right half of the converter;



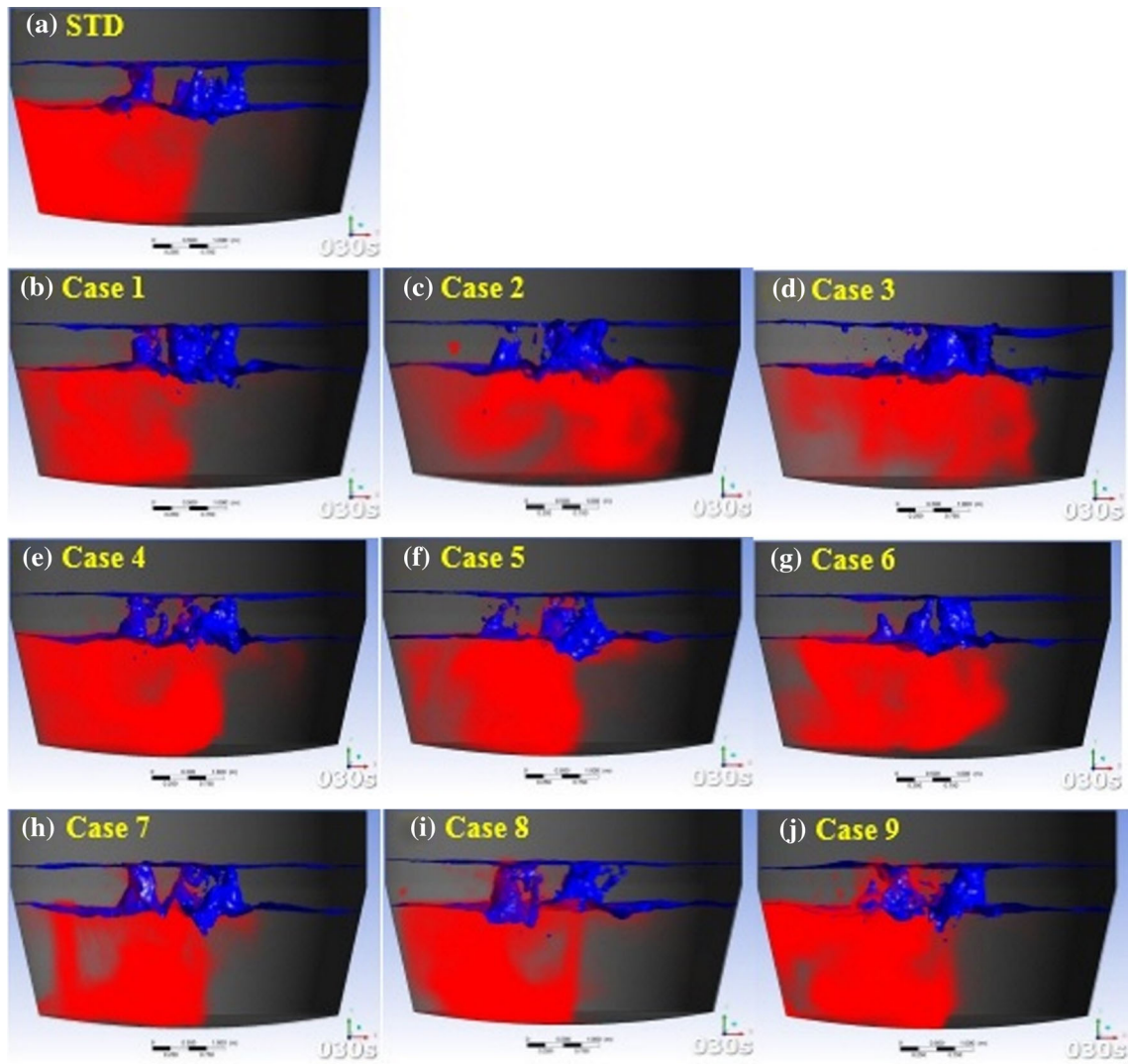


Fig. 9—Distribution of the tracer concentration at 30 s in the ten cases.

in particular, the tracer distributions in Cases 2 and 3 were wider than that in other cases. At 40 seconds (Figure 10), the tracer in STD, Case 1, and the V-type patterns (Cases 7 to 9) began to flow to the right half of the converter. The tracer flow in STD and Case 1 were slower than that in the other cases. The tracer in Cases 2 and 3 had nearly spread throughout the entire converter by 60 seconds (Figure 11). The STD and Case 1 had a low tracer concentration (indicated in light red) on the right side of the converter at 80 seconds (Figure 12).

In quantitative analysis, mixing time is typically defined as the time at which the degree of uniformity  $U$  of the tracer concentration at the detection point ranges between 0.95 and 1.05.<sup>[23]</sup> The degree of uniformity is defined as

$$U = \frac{C_i}{C_0}, \quad [6]$$

where  $C_0$  is the equilibrium concentration and  $C_i$  is an instantaneous concentration.

Figure 13 shows the variations of STD tracer concentration with time. The color gradients corresponding to tracer concentrations from 10 to 170 seconds with a 20-second interval are shown in Figure 13(a). The red, orange, yellow, green, and blue colors in the figure represent descending concentration levels. This type of expression obviously depicted the differences in the concentrations throughout the entire converter. In Figure 13(b), red and blue curves represent the detection point concentrations on the left and right sides, respectively. Thus, the mixing time for STD can be inferred to be 184.7 seconds.

Figure 14 shows the mixing time of the ten cases, for which analysis and comparison results are as follows: (1) The mixing efficiency of linear bottom blowing flow rate distribution patterns (Parts 1 and 2) and V-type patterns (Part 3) was higher than that of uniform patterns (STD). Moreover, the mixing efficiency of linear distribution patterns was higher than that of V-type patterns. These simulation results were identical to the water model

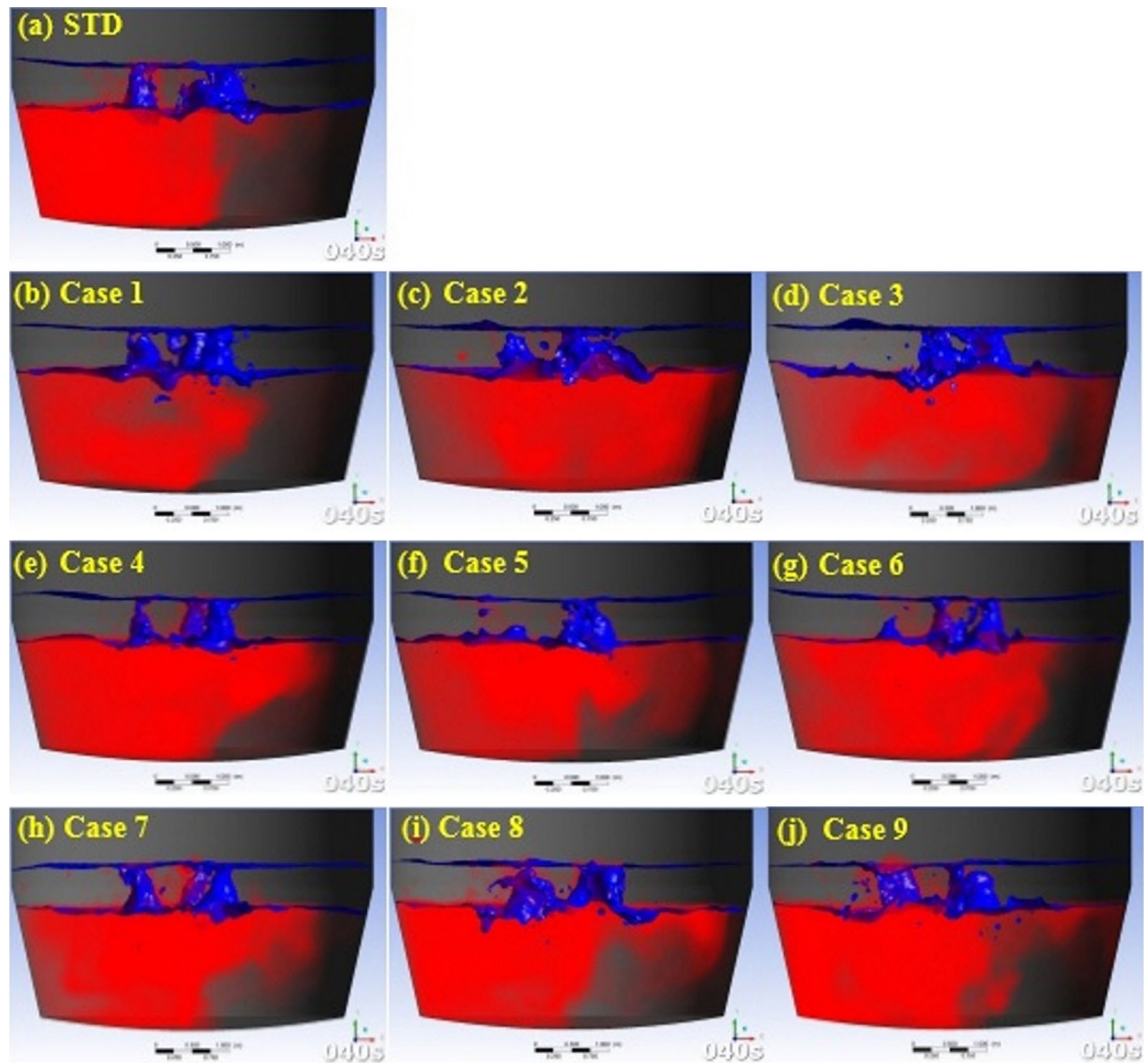


Fig. 10—Distribution of the tracer concentration at 40 s in the ten cases.

experiment by Singh *et al.*<sup>[12]</sup> indicating that the mixing efficiency was highest in linear patterns, followed by V-type patterns and then uniform patterns. (2) The linear distribution pattern of the fixed total flow rate (Part 1) indicated that increasing the bottom blowing flow rate gradients from STD to Case 2 (STD → Case 1 → Case 2) facilitated a reduced mixing time. However, when the gradient exceeded a certain degree (Case 3), the mixing efficiency could not be further improved. In other words, when the bottom blowing flow rate gradient reached a critical value, the mixing efficiency no longer increased with the gradients. (3) Among the linear distribution patterns with a fixed maximal flow rate at 80 Nm<sup>3</sup>/h (Part 2), Case 6 exhibited the shortest mixing time of 117.4 seconds. The mixing time of Cases 4 and 5 were approximately 131 seconds. Although the total flow rate of Part 2 was lower, particularly in Case 6, which had the lowest, the mixing time was shorter than that of STD, V-type patterns, and Case 1. This result suggested that despite the decreased total flow rates, the linear distribution patterns combined with

effective gradients could enhance the mixing efficiency. Literature<sup>[13]</sup> emphasized that if the bottom blowing flow rate distribution was poorly designed, a large bottom blowing flow rate would not result in increased mixing efficiency. The simulation results of the mixing times in the ten cases indicated that the mixing efficiency was most favorable when the bottom blowing flow rate distribution pattern was linear, gradients were large, and bottom blowing total flow rates were substantial (*i.e.*, Cases 2 and 3). The second most favorable was Case 6, which exhibited a linear bottom blowing flow rate distribution pattern, effective gradients, and a low bottom blowing total flow rate. Using STD as a reference point, the mixing efficiency of the other nine cases increased within the range of 18 to 57 pct.

#### E. Liquid Steel–Slag Interface Velocity and Dynamic Pressure

A study<sup>[13]</sup> suggested that linear bottom blowing flow rate distribution resulted in superior mixing efficiency

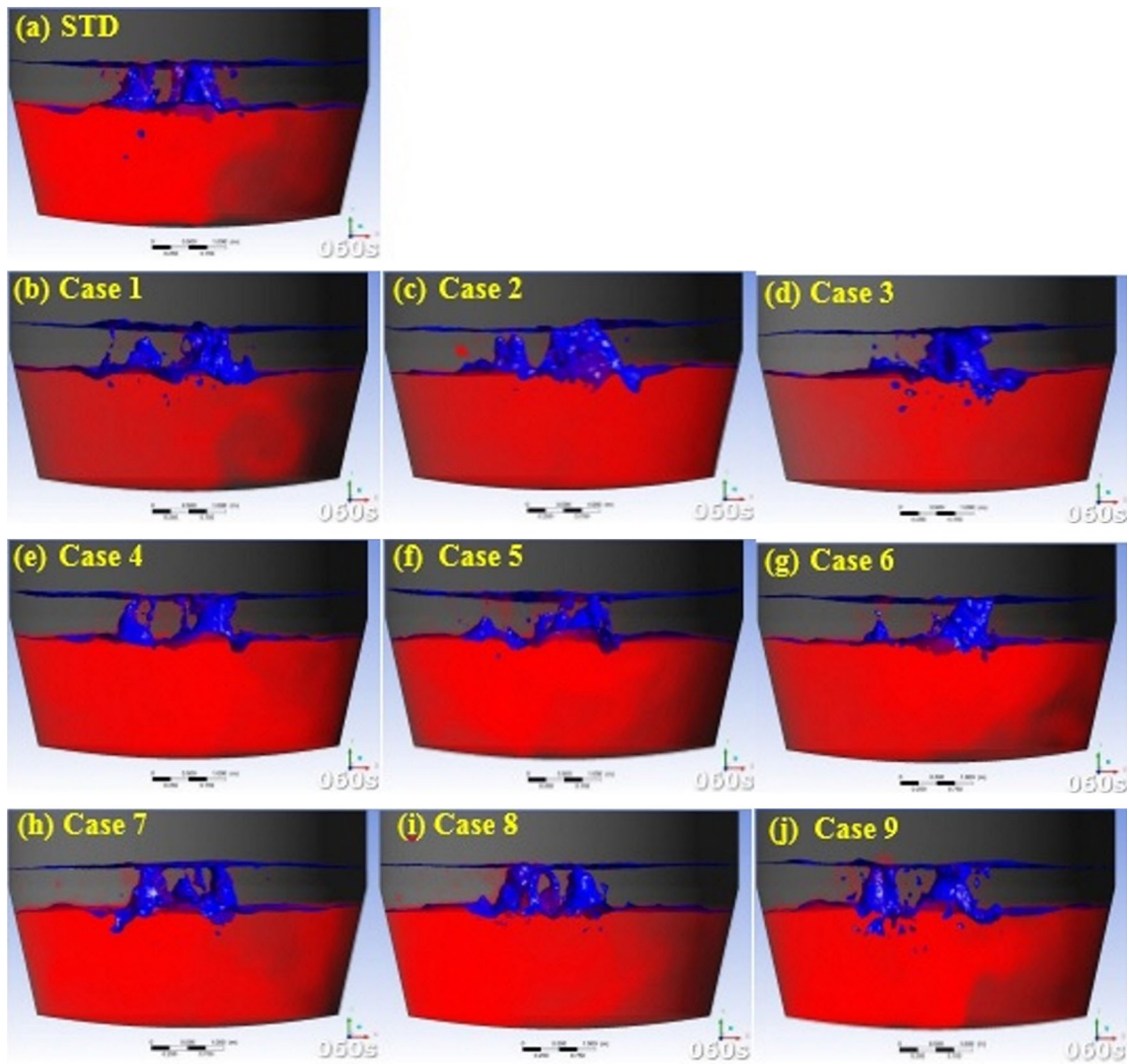


Fig. 11—Distribution of the tracer concentration at 60 s in the ten cases.

because a large radial velocity existed inside the converter. Thus, the current study involved calculating the average radial velocity of liquid steel in each case. Figure 15 depicts that in Part 1, linear bottom blowing flow rate distribution patterns caused larger radial velocity than did the uniform and V-type patterns with the same total flow rates. Comparing Cases 1 to 3 suggested that the radial velocity increased with the bottom blowing flow rate gradients.

Figure 16 shows the average velocity of the liquid steel–slag interfaces in the ten cases to evaluate the stirring force between slag and liquid steel. The average velocity was obtained by averaging velocities of the grids in the liquid steel–slag interfaces. Comparing Cases 4 to 6 in Part 2 indicated that the interface velocity decreased as the bottom blowing total flow rates decreased. A comparison of Part 2 with Parts 1 and 3 also revealed the relevance between interface velocity and bottom blowing total flow

rates mentioned above. With the same total flow rate conditions (Parts 1 and 3), when the bottom blowing flow rate distribution gradients increased in Cases 1 to 3, the flow rate in the right-side bottom tuyeres increased, generating increased interface velocity. Among the ten cases, the interface velocity was the highest in Case 3 because of the substantial bottom blowing total flow rates ( $480 \text{ Nm}^3/\text{h}$ ) and the highest flow rates in the right-side bottom tuyeres ( $140 \text{ Nm}^3/\text{h}$ ). These results indicated that the average liquid steel–slag interface velocity was primarily affected by the bottom blowing total flow rates and distribution gradients. Figure 17 illustrates a gradient map of the liquid steel–slag interface velocity at 100 seconds. In the figure, the interface velocity in Part 2 was lower than that in STD and Parts 1 and 3. From left to right, in Parts 1 and 3, the red regions indicating high velocity increased, a trend that is consistent with the quantitative calculation tendency.

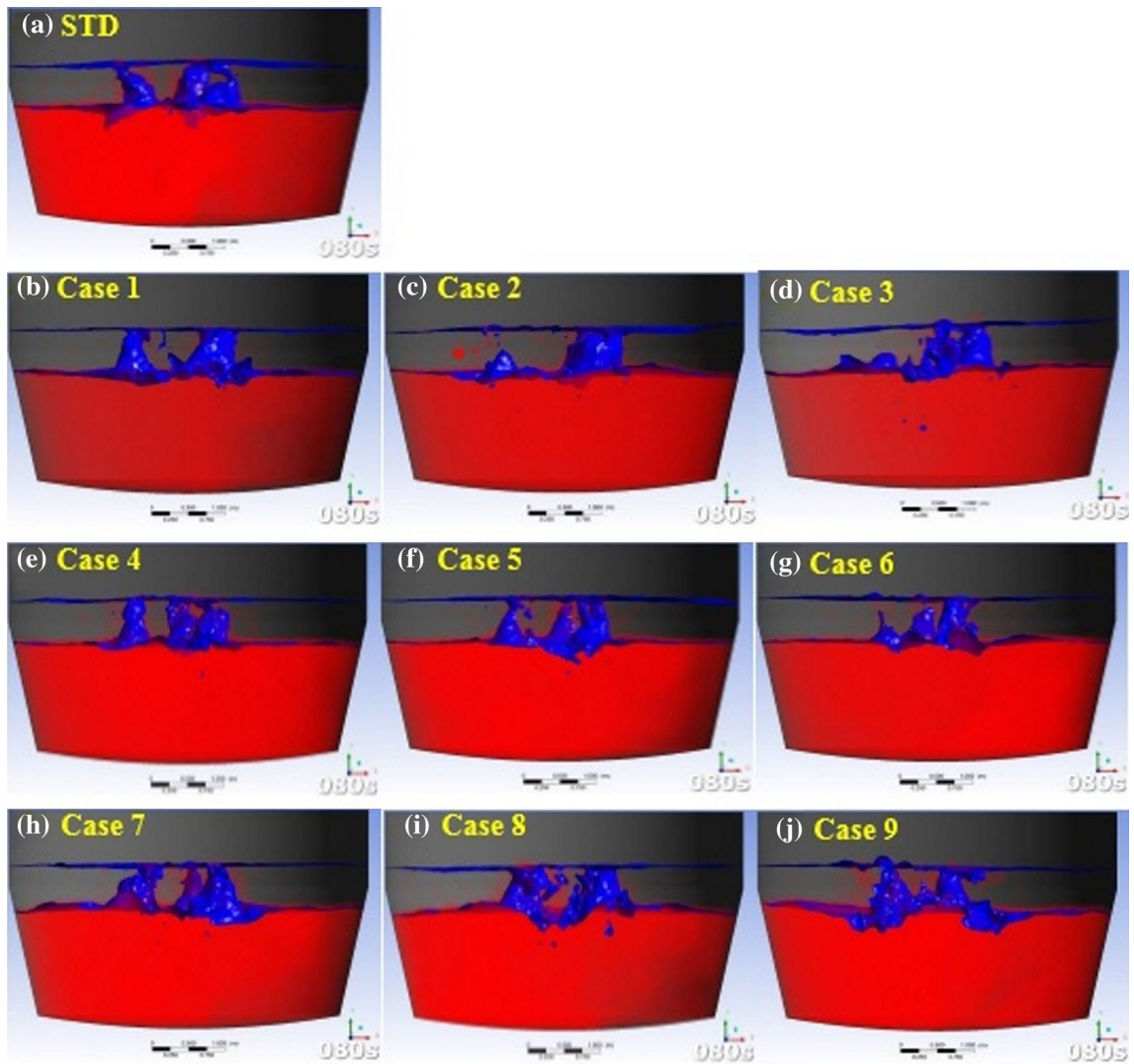


Fig. 12—Distribution of the tracer concentration at 80 s in the ten cases.

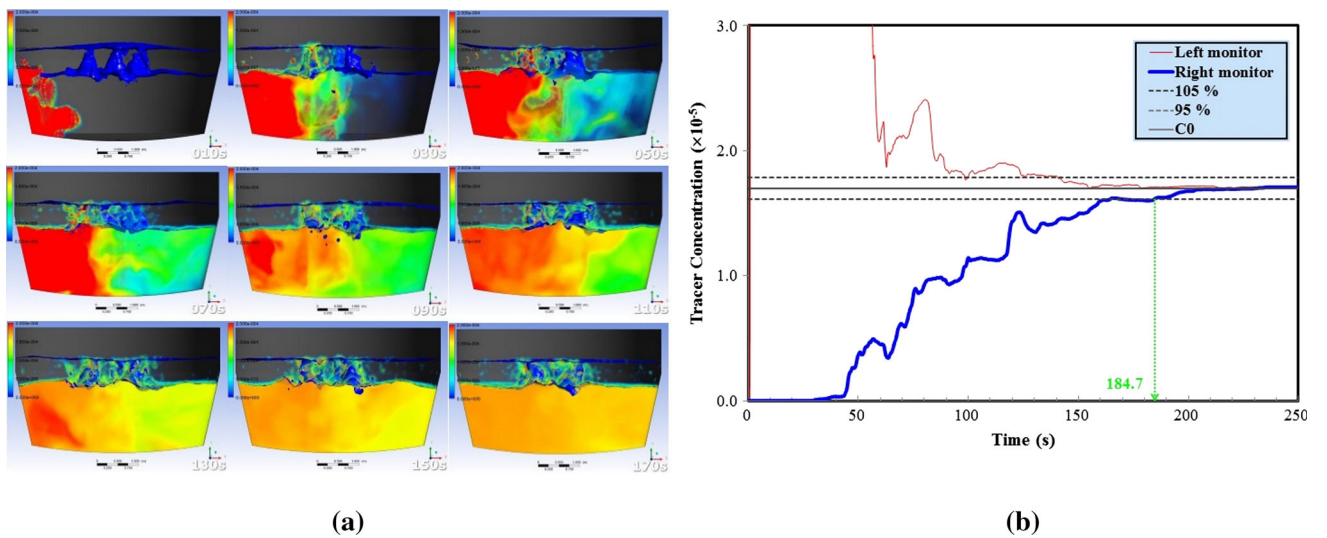


Fig. 13—Mixing time of STD (*a*) from left to right and top to bottom, showing the qualitative analysis performed from 10 to 170 s with a 20-s interval; (*b*) quantitative analysis.

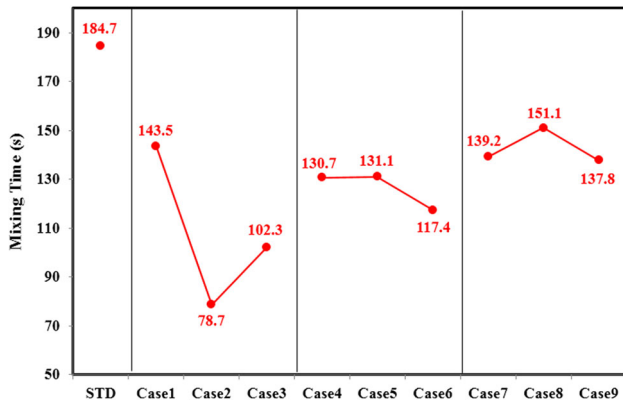


Fig. 14—Mixing time of the ten cases.

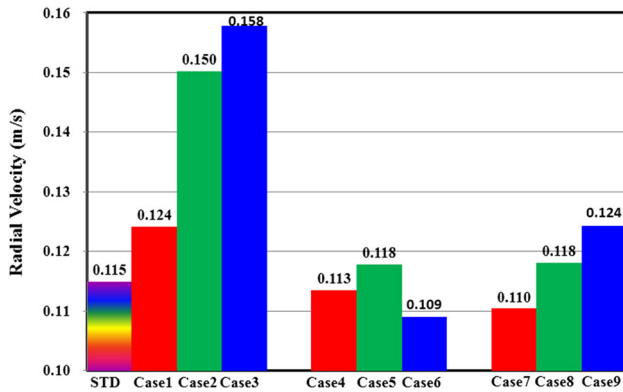


Fig. 15—Average radial velocity of liquid steel.

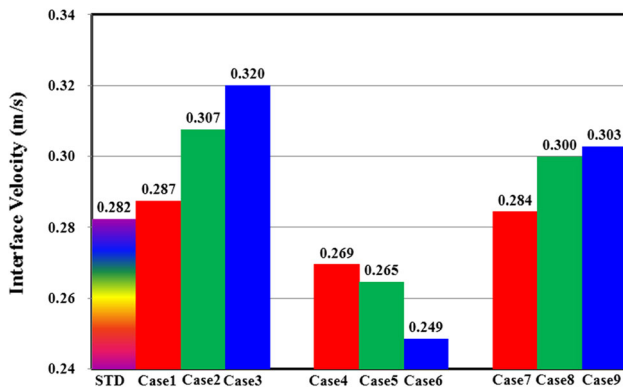


Fig. 16—Average velocity of the liquid steel–slag interface.

## IV. CONCLUSIONS

This study first created a 3D multiphase simulation system to address converter processes. The simulation system was used to conduct ten numerical experiments and analyze the effects of the bottom blowing gas flow rate distribution patterns (uniform, linear fixed total flow rate, linear fixed maximal flow rate, and V-type)

and bottom blowing flow rate distribution gradients exerted on the slag surface stirring heights, flow field patterns, dynamic pressure of the simulation system, mixing time, and liquid steel–slag interface velocity. Based on the simulation results, the following conclusions were obtained.

### A. Slag Surface Stirring Height

1. Slag surface stirring heights were primarily affected by the bottom blowing flow rate distribution patterns and gradients.
2. Stirring in two linear patterns was greater than that in V-type patterns.
3. When the bottom blowing flow rate distribution patterns were identical, more stirring was caused by more bottom blowing flow rate gradients.

### B. Dynamic Pressure of the Simulation System

1. The dynamic pressure of the liquid steel + slag system increased with the total flow rate.
2. The linear bottom blowing flow rate distribution patterns exhibited higher dynamic pressure than did the V-type patterns.
3. The system dynamic pressure increased with the bottom blowing flow rate distribution gradients.

### C. Mixing Time

1. The mixing efficiencies, compared according to bottom blowing flow rate distribution patterns, were highest in linear patterns (fixed total flow rate), followed by linear (fixed maximal flow rate), V-type, and uniform patterns.
2. The efficiencies arranged in order by cases are in the following sequence: Case 2 > Case 3 > Case 6 > Case 4 ~ Case 5 > Case 9 ~ Case 7 > Case 1 > Case 8 > STD. Thus, Cases 2 and 3 that had linear bottom blowing flow rate distribution patterns and substantial gradients and bottom blowing total flow rates exhibited the most favorable mixing efficiency.
3. According to Cases 4 to 6, despite having reduced bottom blowing total flow rates, linear bottom blowing flow rate distribution patterns can be combined with effective gradients to increase the mixing efficiency.

### D. Liquid Steel–Slag Interface Velocity

1. The average velocity of the liquid steel–slag interface was primarily affected by the bottom blowing total flow rates and bottom blowing flow rate distribution gradients.
2. The interface velocity was highest in Case 3 because of the high bottom blowing total flow rate ( $480 \text{ Nm}^3/\text{h}$ ) and the highest flow rate in the right-side bottom tuyeres ( $140 \text{ Nm}^3/\text{h}$ ).

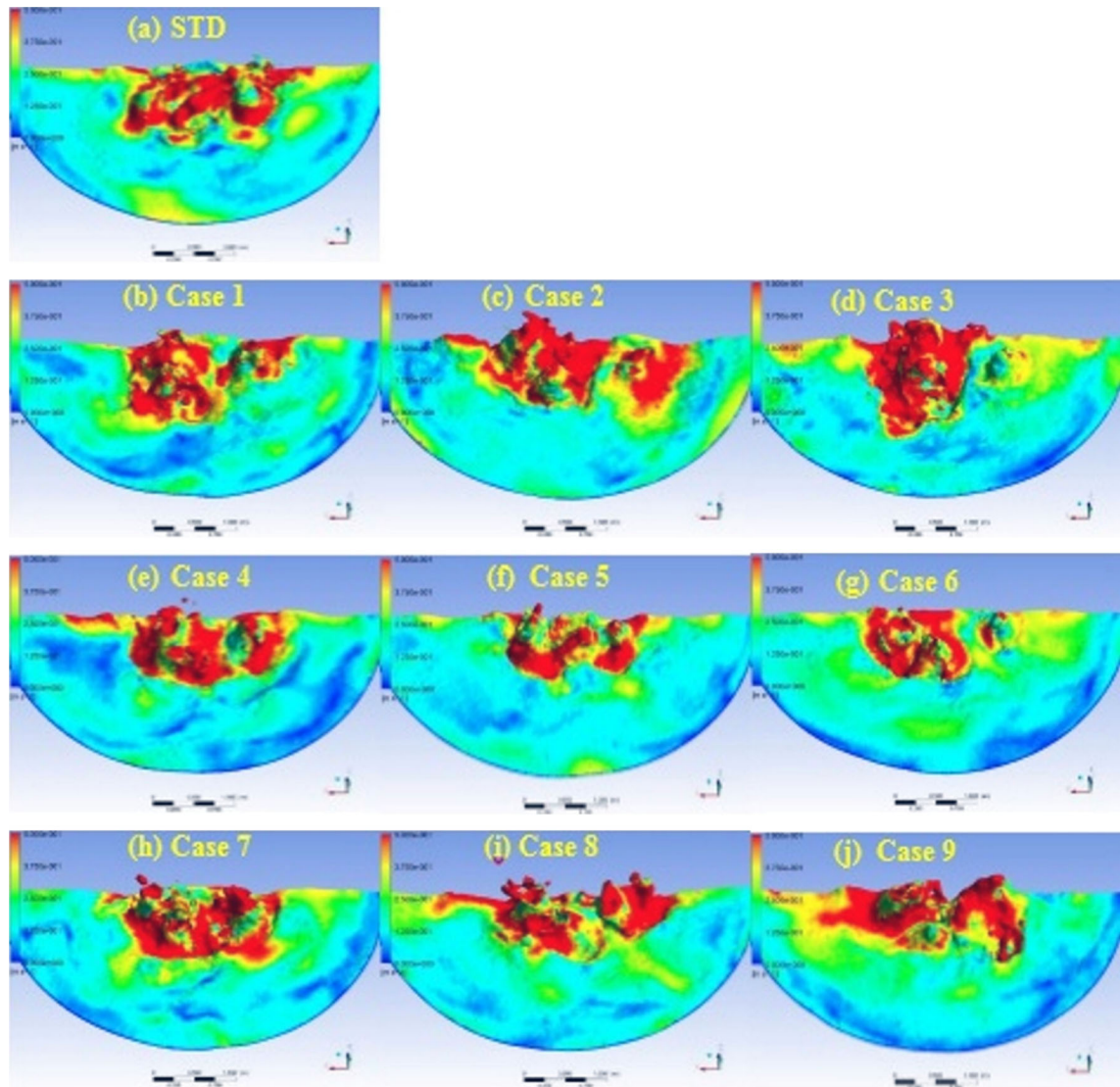


Fig. 17—Velocity gradient map of the liquid steel–slag interface at 100 s.

#### ACKNOWLEDGMENTS

This work was supported by the China Steel Corporation in Taiwan, for which the authors are grateful.

#### CONFLICT OF INTERESTS

The authors declare there are no conflicts of interest.

#### REFERENCES

1. X. Zhou, M. Ersson, L. Zhong, J. Yu, and P. Jönsson: *Steel Res. Int.*, 2014, vol. 85, pp. 273–81.
2. T.M.J. Fabritius, P.T. Kurkinen, P.T. Mure, and J.J. Härkki: *Ironmak. Steelmak.*, 2005, vol. 32, pp. 113–19.
3. M. Lv, R. Zhu, X. Wei, H. Wang, and X. Bi: *Steel Res. Int.*, 2012, vol. 83, pp. 11–15.
4. Y. Li, W.T. Lou, and M.Y. Zhu: *Ironmak. Steelmak.*, 2013, vol. 40, pp. 505–14.
5. M. Lv, R. Zhu, Y.G. Guo, and Y.W. Wang: *Metall. Mater. Trans. B*, 2013, vol. 44B, pp. 1560–71.
6. Q. Li, M. Li, S. Kuang, and Z. Zou: *Metall. Mater. Trans. B*, 2015, vol. 46B, pp. 1494–1509.
7. X. Zhou, M. Ersson, L. Zhong, and P. Jonsson: *Metall. Mater. Trans. B*, 2015. DOI: [10.1007/s11663-015-0465-0](https://doi.org/10.1007/s11663-015-0465-0).
8. L.C. Zhong, X. Wang, Y.X. Zhu, B.Y. Chen, B.C. Huang, and J.X. Ke: *Ironmak. Steelmak.*, 2010, vol. 37, pp. 578–667.
9. S. Ganguly, V. Singh, and S. Chakraborty: *ISIJ Int.*, 2006, vol. 46, pp. 1731–33.
10. S.K. Choudhary and S.K. Ajmani: *ISIJ Int.*, 2006, vol. 46, pp. 1171–76.
11. V. Singh, J. Kumar, C. Bhanu, S.K. Ajmani, and S.K. Dash: *ISIJ Int.*, 2007, vol. 47, pp. 1605–12.
12. V. Singh, S.N. Lenka, S.K. Ajmani, C. Bhanu, and S. Pathak: *ISIJ Int.*, 2009, vol. 49, pp. 1889–94.
13. Z. Lai, Z. Xie, and L. Zhong: *ISIJ Int.*, 2008, vol. 48, pp. 793–98.
14. F. Fluent: *FLUENT 63 User's Guide*, Fluent Inc., Lebanon, NH, 2006.
15. B.E. Launder and D.B. Spalding: *Lectures in Mathematical Models of Turbulence*, Academic Press, London, 1972.

16. J.U. Brackbill, D.B. Kothe, and C. Zemach: *J. Comput. Phys.*, 1992, vol. 100, pp. 335–54.
17. C.W. Hirt, B.D. Nichols, and R.S. Hotchkiss: Report LA-8355, Los Alamos Scientific Laboratory, Los Alamos, NM, August 1980.
18. C.W. Hirt and B.D. Nichols: *J. Comput. Phys.*, 1981, vol. 39, pp. 201–25.
19. D.L. Youngs: in *Numerical Methods for Fluid Dynamics*, K.W. Morton and M.J. Baines, eds., Academic Press, New York, NY, 1982, pp. 273–285.
20. R. Scardovelli and S. Zaleski: *J. Comput. Phys.*, 2000, vol. 164, pp. 228–37.
21. W.J. Rider and D.B. Kothe: *J. Comput. Phys.*, 1998, vol. 141, pp. 112–52.
22. H.J. Odenthal, U. Falkenreck, and J. Schlüter: *Proceedings of the European Conference on Computational Fluid Dynamics*, Egmond aan Zee, The Netherlands, 2006.
23. J. Fang, X. Ling, Z.F. Sang, and Q.B. Yang: *IEEE Conference Publications*, Wuhan, 2010, pp. 479–82.